PHYSICAL REVIEW B **74**, 125321 (2006)

Scattering-assisted terahertz gain in semiconductor superlattices in the Wannier-Stark-Ladder regime

Yu. A. Tarakanov,[1] M. A. Odnoblyudov,[1] K. A. Chao,[2] N. Sekine,[3] and K. Hirakawa[3]
[1]*A. F. Ioffe Physico-Technical Institute, Russian Academy of Science, 194021 St. Petersburg, Russia*
[2]*Division of Solid State Theory, Department of Physics, Lund University, S-223 62 Lund, Sweden*
[3]*Institute of Industrial Science, University of Tokyo, Tokyo 153-8505, Japan*
(Received 15 June 2006; published 28 September 2006)

Using the second-order perturbation theory we have calculated the scattering assisted gain spectra in GaAs/AlGaAs superlattice under a strong applied electric field in the Wannier-Stark-Ladder (WSL) regime. Nonequilibrium distribution function of quasi-two-dimensional carriers localized in each WSL level and indirect optical transitions between neighboring WSL levels accompanied by the emission or absorption of acoustical phonons are taken into account in our theoretical analysis and numerical calculation. We have shown that the experimentally observed down shift of the zero-gain frequency from the Bloch oscillation frequency is due to the inelastic nature of the phonon scattering and the formation of excitons when electron-hole pairs are photoexcited. Our theoretical results agree well with the experimental data which were obtained from analyzing the THz response of superlattices to the picosecond optical pulse excitation.

DOI: 10.1103/PhysRevB.74.125321 PACS number(s): 73.21.Fg, 73.20.Hb

I. INTRODUCTION

The feasibility of making a Bloch oscillator, which emits electromagnetic radiation in the THz frequency range and is tunable with external electric field, has been much investigated, but some important questions still remain to be answered. Soon after the original proposal by Esaki and Tsu[1] on generating Bloch oscillation (BO) in semiconductor superlattices, Ktitorov *et al.*,[2] Romanov[3] and Ignatov[4] predicted possible optical gain from such BO. By solving the kinetic equation in the relaxation time approximation, one can show a resonancelike behavior of the real part of the complex conductivity with its peak position somewhat lower than the BO frequency ω_B. It turns into an absorption behavior at frequencies higher than ω_B. The frequency at which the gain vanishes depends on the relaxation time.

According to a recent theoretical analysis[5] this type of amplification of THz radiation is associated with the k-space electron bunching, i.e., the accumulation of electron distribution in a localized region in k space. In terms of a miniband description, it was demonstrated[6] that the bunching is mainly mediated by the spontaneous emission of optical phonons by the Bloch oscillating electrons. The amplification of THz radiation was studied with one-dimensional models,[3,4,7] Green's functions approach,[8] and three-dimensional Monte Carlo calculations.[6,9] Willenberg *et al.*[10] investigated the BO related THz gain with the density matrix approach, and the gain formation involves only elastic scattering mechanisms. However, recent experiment described in Sec. II suggested that such an approach does not describe adequately the experimental data. While there are experimental evidences[11–15] for the existence of BO, only recently Sekine and Hirakawa[16] have successfully used the time-domain THz-electrooptic sampling technique to determine directly the spectral shape of the complex conductivities of Bloch oscillating electrons, and demonstrated clearly a dispersive Bloch gain in semiconductor superlattices.

When the applied electric field increases to a threshold value $F_0=\hbar/ed\tau$, where τ is the relaxation time and d the superlattice constant, the separation $\hbar\omega_B$ between the electron eigenenergies becomes equal to the level broadening $\hbar/\tau$ induced by the scattering. With further increase of the electric field, the electron eigenenergies form a Wannier, Stark, Ladder (WSL), and the corresponding eigenfunctions in semiconductor superlattices tend to be localized at superlattice sites. Then the miniband transport picture is no longer valid, and the differential drift velocity, or the differential conductance becomes negative, which was pointed out by Esaki and Tsu in their pioneering work.[1] In this WSL localization regime, the scattering-assisted processes are of crucial importance to the understanding of electron transport. Recently a theoretical model of scattering assisted transport[20] was developed which can explain the experimentally observed fine structures in the current voltage characteristics. The dominating mechanism to produce these fine structures is the inelastic scattering between electrons and optical phonons which assists the electrons to move from one WSL localized state to the other WSL localized state. The model allows one to obtain the steady state nonequilibrium momentum distribution function of the carriers in a two-dimensional (2D) energy band associated to each WSL level (or to each superlattice cell). Therefore, with this model one can also study the stimulated optical transitions between two 2D bands associated to two neighboring WSL levels or two neighboring superlattice cells.

In this paper, THz gain arising from scattering assisted indirect optical transitions between neighboring WSL levels is studied as a function of the photon energy and the applied electric field strength. The calculated gain spectra are then compared with the measured data. We will first outline in Sec. II the experiments which provide the THz gain spectra of a GaAs/AlGaAs supperlattice sample. By analyzing the phonon-assisted optical transitions between two WSL levels, the dispersive THz gain spectrum is derived in Sec. III. Here we found that instead of optical phonons which dominate the negative differential conductance, the deformation and piezoelectric acoustical phonons are most influential to the

 ©2006 The American Physical Society

gain spectrum. The frequency at which the gain vanishes is of particular interest in our investigation, and our calculated zero-gain frequency is higher than the measured one. Our study on excitonic effect in Sec. IV explains the down-shift of the zero-gain frequency and brings the theory and experiment to good agreement, which is presented in Sec. V. The conclusion follows in the last Sec. VI.

II. EXPERIMENTS

The sample used in this work was prepared by growing a 500 nm thick undoped $GaAs/Al_{0.3}Ga_{0.7}As$ superlattice layer on an n^+-GaAs substrate by molecular beam epitaxy. The thickness of the GaAs quantum well layers and that of the $Al_{0.3}Ga_{0.7}$ barrier layers were 6.5 nm and 2.5 nm, respectively. The ground miniband of this sample was 30 meV wide and was separated from the first excited miniband by a 100 meV wide minigap. The top and the bottom contacts were formed by depositing a semi-transparent NiCr Schottky film and AuGeNi/Au layers, respectively. By using these two electrodes, a static bias electric field F was applied to the undoped superlattice region. When a femtosecond laser pulse excites the sample, electron-hole pairs are optically injected into the miniband. Due to an applied electric field, the carriers start drifting and a THz electromagnetic wave that is proportional to the carrier acceleration is emitted into free space.

The THz radiation was detected by using THz-EO sampling technique.[17,18] In our experiment, a 100 μm thick ZnTe crystal was used as the EOX, which has a rather flat response up to 4 THz. In the EOX, a birefringence proportional to the amplitude of an electric field (Pockels effect) is induced by an incident THz radiation. The wave form of the THz electric field was obtained in the time domain by the balanced detection of the probe lights polarized along the two principal axes of the EOX. The pump and the probe pulses were delivered from a mode-locked Ti:sapphire laser (pulse width 100 fs). The loosely focused pump beam was incident on the SL surface and its power was set to be 4 mW to minimize the field screening effect by the photoexcited carriers. The pump photon energy was adjusted to be 1.605 eV, which is close to the bottom of the ground miniband. The detection bandwidth of our experimental setup was 4 THz, which was limited both by the characteristics of our 100 μm thick ZnTe EOX and by the energy uncertainty of the femtosecond pump laser pulses. The sample was cooled at the temperature $T=10$ K.

Figure 1 shows the wave forms of the THz electric field, $E_{\mathrm{THz}}(t)$, emitted from the SL sample measured at various values of the electric field F, ranging from 1 to 39 kV/cm. For F between 9 and 29 kV/cm, clear oscillations appear in the trailing part and their period becomes shorter with increasing F. Since we create electrons close to the bottom of the ground miniband, the photoexcited electrons are first accelerated by the electric field and, subsequently, decelerated when they go beyond the inflection point of the miniband dispersion. They continue this acceleration and/or deceleration cycle due to periodic Bragg reflection until the coherence of the oscillation is lost. Such an anticipated behavior is

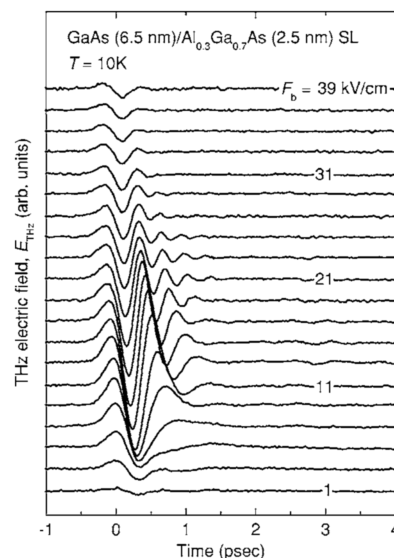

FIG. 1. The wave forms of the THz radiation emitted from the semiconductor superlattice sample recorded for various bias electric fields, F (1–39 kV/cm; 2 kV/cm step). The traces are shifted for clarity.

well reproduced in the $E_{\mathrm{THz}}(t)$ traces. Furthermore, the oscillation period is roughly consistent with the expected Bloch frequency. For the electric field F higher than 25 kV/cm, the oscillatory behavior gradually vanishes because the oscillation frequency exceeds the bandwidth of our measurement setup. The detail of the experiment can be found in Ref. 16.

From a simple argument on the THz emission process from the sample photoexcited by ultrashort optical pulses, the spectral shapes of the dynamical conductivity $\sigma(\omega)$ of Bloch oscillating electrons can be obtained from the Fourier spectra of $E_{\mathrm{THz}}(t)$ traces: the real part $\mathrm{Re}[\sigma(\omega)]$ and the imaginary part $\mathrm{Im}[\sigma(\omega)]$ are proportional to, respectively, the real part $\mathrm{Re}[E_{\mathrm{THz}}(\omega)/F]$ and the imaginary part $\mathrm{Im}[E_{\mathrm{THz}}(\omega)/F]$ of the Fourier spectra of $E_{\mathrm{THz}}(t)/F$. While the details of such type of data analysis can be found in Ref. 16, here we will refer particularly to Figs. 3(a), 3(b) and 3(d) in that paper. In fact, the content in Figs. 3(a) and 3(d) will be shown later in the present paper when we compare our calculated results with the experimental data. Figures 3(a) and 3(b) show $\mathrm{Re}[E_{\mathrm{THz}}(\omega)/F]$ and $\mathrm{Im}[E_{\mathrm{THz}}(\omega)/F]$ obtained from the experimental data plotted in Fig. 1. $\mathrm{Re}[E_{\mathrm{THz}}(\omega)/F]$ has a dispersive curve and shows a negative value up to about 3 THz. This is a clear experimental evidence for the dispersive Bloch gain in semiconductor superlattices. At the crossover frequency $\omega_{\mathrm{exp}}(F)$ where the $\mathrm{Re}[E_{\mathrm{THz}}(\omega)/F]$ trace changes its polarity from negative to positive, $\mathrm{Im}[E_{\mathrm{THz}}(\omega)/F]$ shows a clear dip. At the crossover frequency $\omega_{\mathrm{exp}}(F)$ the gain is zero. Because of the electron-phonon interaction, the measured zero-gain frequency $\omega_{\mathrm{exp}}(F)$ is expected to be slightly less than the BO frequency $\omega_B(F)$ which is linear in F. However, the comparison of $\omega_B(F)$ and $\omega_{\mathrm{exp}}(F)$ in Fig. 3(d) indicates that the difference $\omega_B(F)-\omega_{\mathrm{exp}}(F)$ is too large to be explained by the electron-phonon interaction alone. As we will see in the latter part of this paper, the excitonic effect gives the major contribution to this difference $\omega_B(F)-\omega_{\mathrm{exp}}(F)$.

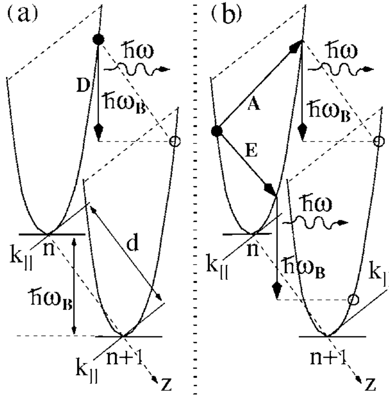

FIG. 2. The schematic illustration of the direct (a) and the indirect (b) optical transitions between two neighboring WSL levels.

III. DISPERSIVE TERAHERTZ GAIN

In a semiconductor superlattice under an applied electric field F along the growth direction which we label as the z axis, negative differential drift velocity (or negative differential conductance) appears when F is larger than its threshold value $F_0=\hbar/ed\tau$. In this WSL localization region with $F>F_0$, we expect interesting features in gain spectra. It is important to notice that in the WSL region the semiclassical theory is no longer valid. Just like using the electron-phonon scattering processes to treat the carrier transport in the WSL region, we should use the photon absorption and (spontaneous or stimulated) photon emission to describe the interaction between electrons and the electromagnetic field.

We will label the eigenenergies as $E_n(\mathbf{k}_\|)=E_n+E(\mathbf{k}_\|)$, where E_n is the WSL energy level associated to the nth superlattice cell with $E_n-E_{n+1}=\hbar\omega_B$, and $E(\mathbf{k}_\|)$ is the 2D energy band. In a process of photon absorption or photon emission, let $E_{n_i}(\mathbf{k}_i)$ be the electron initial state energy and $E_{n_f}(\mathbf{k}_f)$ the electron final state energy. Since the total momentum parallel to interfaces is conserved when an electron transition process occurs with absorption or emission of a photon, we must have $n_i\neq n_f$. There are three electron transition processes which we will illustrate in Fig. 2 using $n_i=n$ and $n_f=n+1$ as an example. Here the WSL levels and the 2D band are plotted schematically with horizontal bars and parabolic dispersions. The part (a) on the left-hand side of Fig. 2 is for the direct process (marked with D) with $\mathbf{k}_i=\mathbf{k}_f$ and the photon energy $\hbar\omega=E_{n_i}(\mathbf{k}_i)-E_{n_f}(\mathbf{k}_f)=\hbar\omega_B$. It was pointed out in Ref. 19 that in the steady state the electron population $f(\mathbf{k}_i)$ in the initial state is equal to the electron population $f(\mathbf{k}_f)$ in the final state. Consequently, there is no gain nor loss, and only spontaneous emission can occur.

The other two transition processes involve the emission or absorption of a phonon, the momentum of which is equal to $\mathbf{k}_i-\mathbf{k}_f$. In these processes the in-plane momentum of the initial will differ from that of the final states. Consequently, the initial and the final states will have different populations, and the system can have a net gain for the photon energies $\hbar\omega<\hbar\omega_B$ but a net loss for the photon energies $\hbar\omega>\hbar\omega_B$. In this section we will use the second-order radiative transitions between the neighboring WSL levels to describe the amplification of radiation in BO systems. To do this, we need to consider photon propagation through a biased semiconductor superlattice. We will show that the Bloch electrons can interact only with the photons whose electric-field component is polarized along the growth direction z axis.

While optical phonons play an important role in the understanding of the observed fine structures in the current-voltage curves,[20] here the relevant scattering assisted processes involve mainly acoustical phonons. Let $H_{e\text{-}r}$ and $H_{e\text{-}ph}$ be, respectively, the electron-photon and the electron-phonon interaction Hamiltonians. Using the second order perturbation theory, we can calculate the electron transition rate $W_{n_i\mathbf{k}_i,n_f\mathbf{k}_f}$ from the initial state $|n_i\mathbf{k}_i\rangle$ to the final state $|n_f\mathbf{k}_f\rangle$ when interacting with both photons and phonons. The rate of emitting a photon of energy $\hbar\omega$, accompanied by the emission or absorption of a virtual acoustical phonon, can be written as

$$W_{n_i\mathbf{k}_i,n_f\mathbf{k}_f}=\frac{2\pi}{\hbar}\sum_{\mathbf{q}}\left|\frac{\langle n_i\mathbf{k}_i|H_{e\text{-}ph}|n_m\mathbf{k}_m\rangle\langle n_m\mathbf{k}_m|H_{e\text{-}r}|n_f\mathbf{k}_f\rangle}{E_{n_i}(\mathbf{k}_i)-E_{n_m}(\mathbf{k}_m)-\imath\gamma}\right| \times\left(N_{\mathbf{q}}+\frac{1}{2}\pm\frac{1}{2}\right)\delta[E_{n_i}(\mathbf{k}_i)-E_{n_f}(\mathbf{k}_f)-\hbar\omega\mp\hbar s|\mathbf{q}|], \quad (1)$$

where $\hbar s|\mathbf{q}|$ is the acoustical phonon energy expressed in terms of the speed of sound s, and

$$N_{\mathbf{q}}=\left[\exp\left(\frac{\hbar\omega_{\mathbf{q}}}{k_BT}\right)-1\right]^{-1}$$

is the number of acoustical phonons with wave vector $\mathbf{q}$ at the temperature T. The level broadening of the initial state, γ is produced by different scattering mechanisms which contribute significantly to the electron dynamics in semiconductor superlattices,[20] such as acoustical phonons, optical phonons, alloy disorder and interface roughness scattering. Symbolically we denote $W^l_{n_i\mathbf{k}_i,n_f\mathbf{k}_f}$ for the transition rate due to the lth type of these scattering mechanisms. Then, γ can be expressed as

$$\gamma(\mathbf{k_i})=2\pi\hbar\sum_{l,n_f,\mathbf{k_f}}W^l_{n_i\mathbf{k}_i,n_f\mathbf{k}_f}. \quad (2)$$

In terms of the transition rate and the electron distribution function $f_n(\mathbf{k})$, the emission probability $R^e(\hbar\omega)$ and the absorption probability $R^a(\hbar\omega)$ of a photon with energy $\hbar\omega$ are calculated as

$$R^e(\hbar\omega)=\frac{2}{V}\sum_{n_i,\mathbf{k}_i,n_f,\mathbf{k}_f}W_{n_i\mathbf{k}_i,n_f\mathbf{k}_f}f_{n_i}(\mathbf{k}_i)[1-f_{n_f}(\mathbf{k}_f)], \quad (3)$$

$$R^a(\hbar\omega)=\frac{2}{V}\sum_{n_i,\mathbf{k}_i,n_f,\mathbf{k}_f}W_{n_i\mathbf{k}_i,n_f\mathbf{k}_f}f_{n_f}(\mathbf{k}_f)[1-f_{n_i}(\mathbf{k}_i)], \quad (4)$$

where V is the volume of the system. For the direct transition illustrated by the part (a) of Fig. 1, $R^e(\hbar\omega)=R^a(\hbar\omega)$ because $f_{n_i}(\mathbf{k}_i)=f_{n_f}(\mathbf{k}_f)$. Let us define $I_0(\hbar\omega)=\hbar\omega^2nA_0^2/8\pi c$ as the energy flux carried by the incident photons with energy $\hbar\omega$, where c is the speed of light in vacuum, n the refraction

coefficient, and A_0 the vector potential of the electromagnetic field which can be expressed in terms of the photon density. We can then express the gain spectrum as[21]

$$G(\hbar\omega)=\frac{\hbar\omega[R^e(\hbar\omega)-R^a(\hbar\omega)]}{I_0(\hbar\omega)}. \quad (5)$$

From the above equation it is clear that the direct optical transitions do not contribute to gain because for these processes $R^e(\hbar\omega)=R^a(\hbar\omega)$.

In the following we will give the matrix elements $|\langle n_i\mathbf{k}_i|H_{e\text{-}ph}|n_m\mathbf{k}_m\rangle|$ for the electron-acoustical-phonon interaction with $n_m=n_i$ (intra-WSL-level transition), and $|\langle n_m\mathbf{k}_m|H_{e\text{-}r}|n_f\mathbf{k}_f\rangle|$ for the electron-photon interaction with $n_m\neq n_f$ (inter-WSL-level transition). Here we have neglected the electron-optical-phonon interaction because the appearance of a large optical phonon energy in the denominator of Eq. (1) makes the contribution of this process insignificant.

A. Electron-phonon interaction

In semiconductor superlattices, electrons and acoustical phonons are coupled mainly by deformation potential coupling and piezoelectric coupling. Let $\mathbf{q}_\parallel$ and q_z be the components of phonon wave vector $\mathbf{q}$ parallel and perpendicular to interfaces. The electron-acoustical-phonon interaction matrix element is derived in the form

$$|\langle n_i\mathbf{k}_i|H_{e\text{-}ph}|n_i\mathbf{k}_m\rangle|=[|C(\mathbf{q})|^2_{dp}+|C(\mathbf{q})|^2_{pe}]\delta_{\mathbf{k}_i\pm\mathbf{q}_\parallel,\mathbf{k}_m}\times\left|\int_{-\infty}^{\infty}|\psi^e_{n_i}(z)|^2\exp(\imath q_z z)dz\right|^2, \quad (6)$$

where $\psi^e_{n_i}(z)$ is the electron wave function along the growth direction z axis.

For semiconductors with zinc-blende structures the coupling functions were derived as[22]

$$|C(\mathbf{q})|^2_{dp}=\frac{D^2\hbar}{2V\rho s}q \quad (7)$$

for deformation-potential coupling, where ρ is the mass density and D the deformational potential constant, and

$$|C(\mathbf{q})|^2_{pe}=\frac{8\pi^2e^2\hbar P^2}{V\kappa^2_\infty\rho}\frac{K_h^2}{\omega_\mathbf{q}} \quad (8)$$

for piezoelectric coupling, where κ_∞ is the high frequency dielectric constant. The piezoelectric constant P can be expressed in terms of the third rank piezoelectric tensor elements as $P=2e_{123}=2e_{14}$. For the deformational-potential coupling to acoustical phonons, we retain only the dominating longitudinal mode. However, all polarization modes contribute to the piezoelectric coupling between electrons and acoustic phonons. For this case, we follow Ref. 22 to approximate K_h^2 with its average $\widetilde{K_h^2}$ over the direction of $\mathbf{q}$.

B. Electron-photon interaction

The matrix element of the electron-photon interaction Hamiltonian $H_{e\text{-}r}$ has the standard form

$$\langle n_m\mathbf{k}_m|H_{e\text{-}r}|n_f\mathbf{k}_f\rangle=\left(\frac{eA_0}{m^*c}\right)^2\langle n_m\mathbf{k}_m|\mathbf{e}\cdot\hat{\mathbf{p}}|n_f\mathbf{k}_f\rangle, \quad (9)$$

where m^* is the electron effective mass, $\mathbf{e}$ is the unit vector of photon polarization, and $\hat{p}$ is the momentum operator. Since the system is cylindrically symmetrical around z direction, among the three terms $e_x\hat{p}_x$, $e_y\hat{p}_y$, and $e_z\hat{p}_z$ of the product $\mathbf{e}\cdot\hat{\mathbf{p}}$, the matrix elements of $e_x\hat{p}_x$ and $e_y\hat{p}_y$ vanish. Using the relation $e_z\hat{p}_z=(Hz-zH)$, the matrix element of the electron-photon interaction can be written as

$$|\langle n_m\mathbf{k}_m|H_{e\text{-}r}|n_f\mathbf{k}_f\rangle|=(\hbar\omega_B)^2\left(\frac{eA_0}{\hbar c}\right)^2\times\delta_{\mathbf{k}_m,\mathbf{k}_f}\left|\int_{-\infty}^{\infty}[\psi^e_{n_m}(z)]^*z\psi^e_{n_f}(z)dz\right|^2. \quad (10)$$

C. Numerical results

The dominating transition process with the emission or absorption of one photon involves the transfer of an electron between two neighboring wells in the superlattice. Hence, we set $n_m=n_i$ and $n_f=n_i+1$. The transition rate can now be set in the final form

$$W_{n_i\mathbf{k}_i,n_f\mathbf{k}_f}=\frac{2\pi}{\hbar}\sum_{q_z}\sum_{q_\parallel}\delta_{\mathbf{k}_i\pm\mathbf{q}_\parallel,\mathbf{k}_m}\delta_{\mathbf{k}_m,\mathbf{k}_f}\times\frac{[|C(\mathbf{q})|^2_{dp}+|C(\mathbf{q})|^2_{pe}](eA_0\omega_B/c)^2}{[\hbar^2(k_i^2-k_m^2)/2m^*]^2+\gamma(\mathbf{k}_i)^2}\times\left|\int_{-\infty}^{\infty}|\psi^e_{n_i}(z)|^2\exp(\imath q_z z)dz\right|^2\times\left|\int_{-\infty}^{\infty}[\psi^e_{n_i}(z)]^*z\psi^e_{n_i+1}(z)dz\right|^2\left(N_\mathbf{q}+\frac{1}{2}\pm\frac{1}{2}\right)\times\delta\left(\frac{\hbar^2(k_i^2-k_f^2)}{2m^*}+\hbar\omega_B-\hbar\omega\mp\hbar s|\mathbf{q}|\right). \quad (11)$$

To calculate the above transition rate, we need to know the wave functions $\psi^e_{n_i}(z)$ associated to the n_ith well in the superlattice, and the level broadening $\gamma(\mathbf{k}_i)$. We obtain the wave functions using the computation scheme given in Ref. 23. Besides the level broadening $\gamma(\mathbf{k}_i)$, we also need to know the nonequilibrium distribution function $f_{n_i}(\mathbf{k}_i)$ in order to be able to calculate the emission probability Eq. (4) and the absorption probability Eq. (5). $f_{n_i}(\mathbf{k}_i)$ and $\gamma(\mathbf{k}_i)$ are derived with the Monte Carlo simulation procedure which is described in Ref. 20.

The so calculated gain spectrum $G(\hbar\omega)$ for an applied electric field $F=17$ V/cm is plotted in Fig. 3 as the dotted curve. The zero-gain frequency (ZGF) $\omega_{th}(F)$ at which $G[\hbar\omega_{th}(F)]=0$ is the calculated field-dependent BO frequency. Because of the inelastic scattering, the calculated $\omega_{th}(F)$ is lower than the ideal BO frequency ω_B, as expected. The gain spectra have a resonancelike behavior, changing from positive to negative at ZGF. Since the gain is propor-

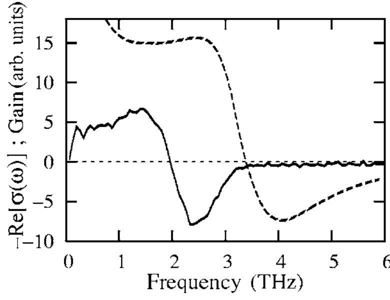

FIG. 3. The calculated gain spectrum (dashed curve) and the measured real part of the complex differential conductivity (solid curve) for an applied electric field 17 kV/cm.

tional to the real part of the complex differential conductivity $\sigma(\omega)$ through the formula[10]

$$G(\hbar\omega) = -\frac{1}{nc}\,\mathrm{Re}[\sigma(\omega)], \tag{12}$$

where n is the carrier concentration, for comparison we have also plotted the measured $\mathrm{Re}[\sigma(\omega)]$ in Fig. 3 as the solid curve. The measured ZGF $\omega_{\mathrm{exp}}(F)$ is substantially lower than $\omega_{th}(F)$, the origin of which will be explained in the next section as the excitonic effect. We also notice that in the low frequency regime, the measured $\mathrm{Re}[\sigma(\omega)]$ is much suppressed. We will explain this phenomenon in the latter part of this paper.

IV. EXCITONIC EFFECT

To perform our experiment, an electric field F is applied first to the semiconductor superlattice sample to generate a WSL energy level structure for electrons and a WSL energy level structure for holes, which are shown in Fig. 4 by the two series of horizontal solid lines. In each WSL the neighboring levels are separated by the BO energy $\hbar\omega_B$. When an electron-hole pair is created by the pumping laser, depending on the laser frequency, the electron and the hole can be in the same well or in different wells. Let the electron be in the n_eth well with the WSL level energy $E^e_{n_e}$, and the hole in the n_hth well with the WSL level energy $E^h_{n_h}$. Due to the Coulomb attraction between the electron and the hole, an exciton is formed with its binding energy $E^{ex}_{(n_e\text{-}n_h)}$ depending on n_e-n_h. Each binding energy is marked as the separation between a pair of horizontal solid and dashed lines. As an illustrating example, $E^{ex}_{(0)}$, $E^{ex}_{(1)}$, and $E^{ex}_{(2)}$ are indicated in Fig. 4. It is important to notice that the separation between two neighbor horizontal dashed lines is not equal to the BO energy $\hbar\omega_B$.

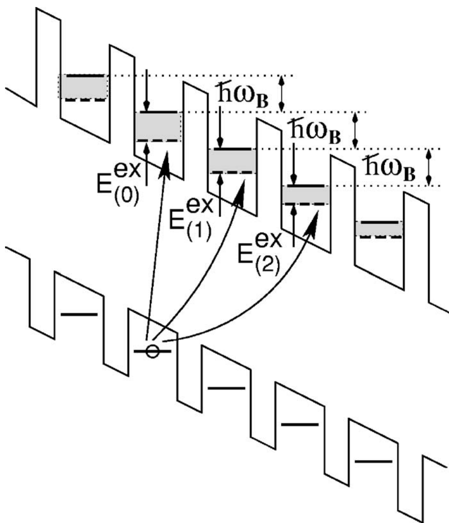

FIG. 4. Photoexcited electron-hole pair forms an exciton with its binding energy depending on the spatial separation between the electron and hole pair. Various binding energies are indicated by the widths of the shaded regions between solid and dashed horizontal lines.

We will use the effective mass approximation to calculate these exciton energies in the WSL localized regime. Let the electron variables be labeled by subscript e, and the hole variables be labeled by subscript h. In the xy-plane parallel to interfaces, we ignore the center of mass variables, and define x,y and p_x,p_y the relative coordinate and relative momentum operators. The Hamiltonian of the interacting electron-hole pair can then be expressed as

$$H^{ex} = p_{ze}^2/2m_e^* + p_{zh}^2/2m_h^* + (p_x^2 + p_y^2)/2\mu - (e^2/\kappa)[x^2 + y^2 + (z_e\text{-}z_h)^2]^{-1/2} + V_C(z_e) + V_C(z_h), \tag{13}$$

where κ is the relative dielectric constant, and μ the reduced electron-hole mass in the xy plane. $V_C(z_e)$ and $V_C(z_h)$ are the confinement potentials for the electron and the hole, respectively, including the contribution from the applied electric field. We have neglected the weak image force effect because of the small difference of dielectric constants in GaAs and in AlGaAs.

We will follow the commonly used variational approach to calculate the exciton binding energy $E^{ex}_{(n_e\text{-}n_h)}$. The electron wave function $\psi^e_{n_e}(z_e)$ and the hole wave function $\psi^h_{n_h}(z_h)$ along the z axis can be calculated with the computation scheme given in Ref. 23 as mentioned in the preceding section. Introducing a normalized function

$$F(z_e\text{-}z_h,\rho) = C\exp(-\lambda\sqrt{\rho^2 + |z_e\text{-}z_h|^2}), \tag{14}$$

where $\rho = \sqrt{x^2+y^2}$ and λ is the variational parameter, the trial function for the exciton is expressed as

$$\Psi^{ex}_{n_e\text{-}n_h}(z_e,z_h,\rho) = \psi^e_{n_e}(z_e)\psi^h_{n_h}(z_h)F(z_e\text{-}z_h,\rho). \tag{15}$$

We should mention that the function $F(z_e\text{-}z_h,\rho)$ can be chosen in different ways. Since here we need only the exciton ground state energy, we choose a hydrogenlike trial function. The exciton binding energy is then calculated as

$$E^{ex}_{(n_e\text{-}n_h)} = E^e_{n_e} + E^h_{n_h} - \langle\Psi^{ex}_{n_e\text{-}n_h}(z_e,z_h,\rho)|H^{ex}|\Psi^{ex}_{n_e\text{-}n_h}(z_e,z_h,\rho)\rangle_{min}, \tag{16}$$

where $\langle\cdots\rangle_{\mathrm{min}}$ is the minimal expectation value. Our calculated exciton binding energy as a function of the applied electric field is plotted in Fig. 5 for n_e-n_h=0 (solid curve),

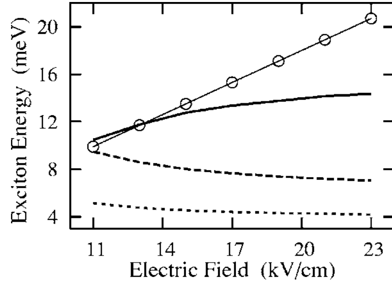

FIG. 5. Exciton binding energies $E^{ex}_{(n_e\text{-}n_h)}$ versus the applied electric field strength: solid curve for n_e-n_h=0, dashed curve for n_e-n_h=1, and dotted curve for n_e-n_h=2. The ideal BO energy $\hbar\omega_B$ is also plotted as the straight line with circles.

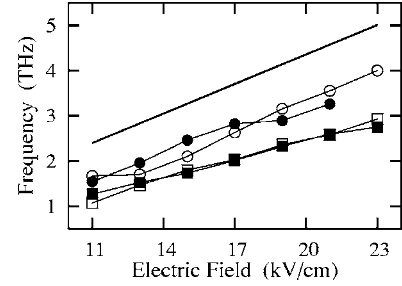

FIG. 6. "Zero-gain" frequency as a function of the applied electric field. The solid symbols are experimental data, and the open symbols are the corresponding theoretical result. The square symbols are for the initial state with the photoexcited electron and hole in the same well, and the circular symbols are for the initial state with the photoexcited electron and hole in two neighboring wells. The straight line is for the BO frequency ω_B.

n_e-n_h=1 (dashed curve), and n_e-n_h=2 (dotted curve). The ideal BO energy $\hbar\omega_B$ is also plotted as the straight line with circles.

With increasing electric field F, the dynamics of the carriers in the semiconductor superlattice goes from the semiclassical regime to the WSL localization regime and then to the Zener tunneling regime. Before reaching the Zener tunneling regime, the single electron wave function $\psi^e_{n_e}(z_e)$ is more localized around the n_eth well for stronger F. Therefore, the overlap between the electron wave function $\psi^e_{n_e}(z_e)$ and the hole wave function $\psi^h_{n_h}(z_h)$ increases with F if $n_e = n_h$, but decrease with F if $n_e \neq n_h$. This is the reason why we see in Fig. 5 the exciton binding energy E^{ex}_0 increases monotonically, but E^{ex}_1 and E^{ex}_2 decrease monotonically when the applied electric field gets stronger. If we increase F further into the Zener tunneling regime, the single particle wave functions begin to delocalize,[24] and the exciton binding energy will have a different field dependence.

We notice that for a given electric field strength, the exciton binding energy $E^{ex}_{(n_e\text{-}n_h)}$ decreases with $|n_e\text{-}n_h|$, and becomes very small for $|n_e\text{-}n_h| \geq 4$. The density of photoexcited electron-hole pairs in our experiment is so low that each exciton is independent of all the others. In this case let us consider once again the problem of optical transition of an electron from one state $\psi^e_{n_i}(z_e)$ associated to the WSL level $E^e_{n_i}$ to the neighboring state $\psi^e_{n_i+1}(z_e)$ associated to the neighboring WSL level $E^e_{n_i+1}$. If we neglect the electron-hole interaction, the energy difference $E^e_{n_i} - E^e_{n_i+1} = \hbar\omega_B$ is independent of the location of the hole wave function $\psi^h_{n_h}(z_h)$. The excitonic effect changes this energy difference into

$$E^e_{n_i} - E^e_{n_i+1} = \hbar\omega_B - (E^{ex}_{(n_i-n_h)} - E^{ex}_{(n_{i+1}-n_h)}). \tag{17}$$

As a result, the BO energy $\hbar\omega_B$ in the delta function in Eq. (11) is replaced by the above expression for $E^e_{n_i} - E^e_{n_i+1}$. This exciton effect will reduce the zero-gain frequency (ZGF) by an amount $E^{ex}_{(n_i-n_h)} - E^{ex}_{(n_{i+1}-n_h)}$.

By tuning the pump laser frequency, one can photoexcite an electron into the $\psi^e_{n_e}(z_e)$ state, leaving a hole in the $\psi^h_{n_h}(z_h)$ state. Experiments have been performed with $|n_e\text{-}n_h|=0$ and $|n_e\text{-}n_h|=1$. The measured ZGF as a function of the applied field F is shown in Fig. 6 for $|n_e\text{-}n_h|=0$ (solid squares) and $|n_e - n_h|=1$ (solid circles). The corresponding theoretical ZGF can be calculated as

$$\hbar\omega_{(1)}(F) = edF - (E^{ex}_0 - E^{ex}_1) \tag{18}$$

for the photoexcited electron and hole in the same well, and

$$\hbar\omega_{(2)}(F) = edF - (E^{ex}_1 - E^{ex}_2) \tag{19}$$

for the photoexcited electron and hole in two neighboring wells. In Fig. 6 the open-squares represent $\omega_{(1)}(F)$, and the open-circles represent $\omega_{(2)}(F)$. As a reference, the BO frequency ω_B is also shown as the straight line. The good agreement between the theory and the experiment strongly suggests the importance of the excitonic effect in the WSL localization regime.

V. THEORY-EXPERIMENT COMPARISON

Based on the formula derived in Sec. III, incorporated with the correction due to the excitonic effect, we have calculated the full gain spectra for the applied electric field F = 11, 13,15, 17, 19, and 21 kV/cm, which are shown in Fig. 7 as dashed curves. In the same figure each corresponding measured real part of the complex differential conductivity $-\text{Re}[\sigma(\omega)]$ is also plotted as a solid curve. For all cases we see the calculated zero-gain frequency coincides with the measured one.

In the high frequency region the absorption part of the calculated spectrum reproduces reasonably the experimental data. However, we notice that in this region the experimental curve exhibits a narrower peak than our theoretical curve. This is due to high-frequency cutoff of our THz measurement system, which arises both from the finite width of our femtosecond laser pulses ($\simeq$100 fs) and the frequency characteristics of our EOX sensitivity. Since the pulse width dt is finite, we cannot induce excitations with frequency component higher than $1/dt$.

When performing experiments, the beam divergence becomes larger and larger as the frequency is lowered. Therefore, it is difficult to detect lower frequency component with-

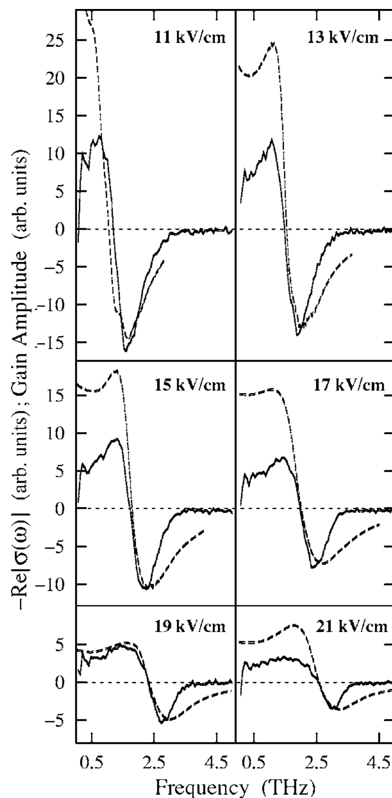

FIG. 7. Experimental values of $-\mathrm{Re}[\sigma(\omega)]$ (solid curves) and calculated gain spectra (dashed curves) at the electric field strength 11, 13, 15, 17, 19, and 21 kV/cm.

out losing its spectral component by using optics (mirrors, etc.) of finite sizes. Therefore, in the low frequency region, the measured gain spectra are expected to be smaller than the calculated ones, because part of the low-frequency component of the THz emission is lost due to the finite aperture of our detection optics. This is exactly what we see in Fig. 7.

VI. CONCLUSIONS

We have performed a theoretical analysis with numerical calculation of the THz radiation amplification in the WSL localization regime in semiconductor superlattice under an applied electric field. We have shown that only indirect optical transitions between two adjacent WSL levels accompanied by the emission or absorption of acoustical phonons can produce the emission or absorption of photons with energy different from the BO energy. Using the second order perturbation theory, our calculated acoustical phonon assisted THz gain spectra exhibit resonant-type structure with maximum somewhat below the BO frequency. The frequency at which the gain spectrum changes sign, namely, the zero gain frequency, is lower than the BO frequency due to two mechanisms: the inelastic nature of the acoustical phonon scattering and the formation of Wannier exciton when an electron-hole pair is photoexcited. The so-created exciton modified the WSL level structure. We have analyzed this phenomenon in detail, and the associated spectra shift is calculated. When the excitonic effect is taken into account, the calculated gain spectra agree well with the experimental data.

To close this paper, we would like to mention the issue of damping of Bloch oscillation which was analyzed by Dmitriev and Suris.[25] In Ref. 25, based on the density matrix formalism, the authors derived a quantum kinetic equation to describe the damping of coherent Bloch oscillations due to scattering. They consider the current as coherent transitions between WSL levels, and the phase factor of the "in" scattering term is responsible for the damping of coherent Bloch oscillations. In our present work, the dc transport of an electron in biased semiconductor superlattices in the WSL regime is treated as a sequence of incoherent scattering events. Therefore, in our analysis there appears no interference process, and no explicit description of the damping of Bloch oscillations.

ACKNOWLEDGMENTS

This work was supported by grants from the Nordic Research Board, the Russian Foundation for Basic Research, and the Dynasty Foundation. The experimental part of this work was supported by the Grant-in-Aid from JSPS, SORST from JST, and IT program from MEXT.

[1] L. Esaki and R. Tsu, IBM J. Res. Dev. **14**, 61 (1970).
[2] S. A. Ktitorov, G. S. Simin, and V. Y. Sindalovskii, Fiz. Tverd. Tela (Leningrad) **13**, 2230 (1971) [Sov. Phys. Solid State **13**, 1872 (1972)].
[3] Yu. A. Romanov, V. Bovin, and L. Orlov, Fiz. Tekh. Poluprovodn. (S.-Peterburg) **12**, 1665 (1978) [Sov. Phys. Semicond. **12**, 987 (1978)].
[4] A. A. Ignatov, K. F. Renk, and E. P. Dodin, Phys. Rev. Lett. **70**, 1996 (1993).
[5] H. Kroemer, cond-mat/0007482 (to be published).
[6] E. Schomburg, N. V. Demarina, and K. F. Renk, Phys. Rev. B **67**, 155302 (2003).
[7] L. K. Orlov and Yu. A. Romanov, Fiz. Tverd. Tela (Leningrad) **19**, 726 (1997) [Sov. Phys. Solid State **19**, 421 (1977)].
[8] A. Wacker and A.-P. Jauho, Phys. Rev. Lett. **80**, 369 (1998); A. Wacker, A.-P. Jauho, S. Rott, A. Markus, P. Binder, and G. H. Döhler, *ibid.* **83**, 836 (1999); A. Wacker, Phys. Rev. B **66**, 085326 (2002).
[9] D. L. Andersen and E. J. Aas, J. Appl. Phys. **44**, 3721 (1973); R. K. Reich, R. O. Grondin, and D. K. Ferry, Phys. Rev. B **27**, 3483 (1983); M. Artaki and K. Hess, Superlattices Microstruct. **1**, 489 (1985).
[10] H. Willenberg, G. H. Döhler, and J. Faist, Phys. Rev. B **67**, 085315 (2003).
[11] J. Feldmann, K. Leo, J. Shah, D. A. B. Miller, J. E. Cunningham, T. Meier, G. von Plessen, A. Schulze, P. Thomas, and S. Schmitt-Rink, Phys. Rev. B **46**, 7252 (1992).
[12] C. Waschke, H. G. Roskos, R. Schwedler, K. Leo, H. Kurz, and

K. Köhler, Phys. Rev. Lett. **70**, 3319 (1993).
[13] T. Dekorsy, P. Leisching, K. Köhler, and H. Kurz, Phys. Rev. B **50**, 8106 (1994).
[14] F. Löser, Y. A. Kosevich, K. Köhler, and K. Leo, Phys. Rev. B **61**, R13373 (2000).
[15] Y. Shimada, K. Hirakawa, and S.-W. Lee, Appl. Phys. Lett. **81**, 1642 (2002).
[16] N. Sekine and K. Hirakawa, Phys. Rev. Lett. **94**, 057408 (2005).
[17] Q. Wu and X.-C. Zhang, Appl. Phys. Lett. **71**, 1285 (1997).
[18] A. Leitenstorfer, S. Hunsche, J. Shah, M. C. Nuss, and W. H. Knox, Appl. Phys. Lett. **74**, 1516 (1999).
[19] G. Bastard and R. Ferreira, C. R. Acad. Sci., Ser. II: Mec., Phys., Chim., Sci. Terre Univers **312**, 971 (1991).
[20] Yu. A. Tarakanov, V. Vettchinkina, M. A. Odnoblyudov, K. A. Chao, N. Sekine, and K. Hirakawa, Phys. Rev. B **72**, 125345 (2005).
[21] Weng W. Chow and Stephan W. Koch, *Semiconductor-Laser Fundamentals* (Springer, New York, 1999), p. 245.
[22] Lin-Wang Wang, Alex Zunger, and Kurt A. Mäder, Phys. Rev. B **53**, 2010 (1996).
[23] Kuijuan Jin, M. Odnoblyudov, Y. Shimada, K. Hirakawa, and K. A. Chao, Phys. Rev. B **68**, 153315 (2003).
[24] A. Vojvodic, A. Blom, Zhongshui Ma, Y. Shimada, K. Hirakawa, and K. A. Chao, Solid State Commun. **136**, 580 (2005).
[25] I. A. Dmitriev and R. A. Suris, Semiconductors **36**, 1364 (2002).